

Superconductivity in laser-annealed monocrystalline silicon films: The role of boron implant

Cite as: Appl. Phys. Lett. **123**, 132602 (2023); doi: [10.1063/5.0166870](https://doi.org/10.1063/5.0166870)

Submitted: 8 July 2023 · Accepted: 6 September 2023 ·

Published Online: 25 September 2023



View Online



Export Citation



CrossMark

P. Dumas,^{1,a)} M. Opprecht,¹ S. Kerdilès,¹ J. Lábár,² B. Pécz,² F. Lefloch,³ and F. Nemouchi¹

AFFILIATIONS

¹Université Grenoble ALPERs, CEA LETI, 38000 Grenoble, France

²Institute for Technical Physics and Materials Science, Centre for Energy Research, Budapest, Hungary

³Université Grenoble ALPERs, CEA IRIG, 38000 Grenoble, France

^{a)} Author to whom correspondence should be addressed: paul.dumas2@cea.fr

ABSTRACT

33 nm thick silicon on insulator films were implanted with boron at high dose (1.5×10^{16} or 2.5×10^{16} at/cm²) and low energy (3 or 4 keV), then further annealed with 160 ns laser pulses. When the laser energy is set such as to lead to the near complete melt of silicon, superconductivity is found in 4 keV-implanted films only, with a critical temperature that increases with dose from 270 to 390 mK. This latter temperature is 200 mK higher than the one recently reported in polycrystalline films of same thickness. Transmission electron microscopy images demonstrate that the films annealed at this particular laser energy are monocrystalline, with a lower density of boron precipitates in superconducting ones at a given dose. A simple model shows that the appearance of superconductivity in 4 keV-implanted films is due to the broader shape of the as-implanted boron distribution.

Published under an exclusive license by AIP Publishing. <https://doi.org/10.1063/5.0166870>

The primitive building block of most advanced quantum processors is made of two superconducting electrodes delimited by a weak link, known as Josephson junction (JJ).^{1–3} In the prospect of building a quantum computer for which a very high number of qubits is required, one is looking for superconductors that ensure the scalable and reproducible fabrication of JJ's.^{1,2} While aluminum is the material of choice in current processors, silicon (Si) is undoubtedly the most appropriate material regarding scalability and reproducibility. Moreover, the Josephson effect has been recently observed in junctions entirely made of silicon, called all-silicon JJ's.⁴ To form the superconducting electrodes of such JJ's, Si is doped with boron well above its solubility limit using gas immersion laser doping (GILD) or pulsed laser induced epitaxy (PLIE).^{5,6} Depending on the technique, boron is introduced through a precursor gas or by ion implantation. In both methods, extremely short laser pulses (~10–100 ns) are employed to electrically activate boron through liquid-phase-epitaxy regrowth (LPER).

Regarding the mass production of all-silicon JJ's, PLIE is more compatible than GILD since it does not require ultra-high vacuum conditions and because ion implantation is a very common technique in the semiconductor industry.⁶ Recently, superconducting silicon on

insulator (SOI) films (33 nm) were obtained from PLIE using a 300 mm-compatible laser anneal system.⁷ The energy and dose of the boron ion implantation were set to 3 keV and 2.5×10^{16} at/cm², respectively. Using 160 ns laser pulses, the complete melt of the SOI layer was found as a required condition to induce superconductivity, leading to polycrystalline films with 170 mK critical temperature (T_C). However, monocrystalline electrodes with higher T_C are desired to boost the supercurrent crossing the JJ's.^{8,9} We here report ion implantation conditions leading to monocrystalline SOI films of higher T_C using the same laser anneal system as in Ref. 7. The role of boron implant on superconductivity is analyzed by coupling standard characterizations and modeling.

Four 300 mm wafers featuring a 15 nm p-type (100) Si layer (5–15 Ω cm) on top of a 20 nm buried oxide (BOX) were used. SOI layers were first thickened up to 33 nm by epitaxy. Then, boron was implanted at tilt 7° and twist 22° using conditions given in Table I. The ion implantation leads to the amorphization of close to half of the SOI layer with slight variations related to dose and energy changes.⁷ Finally, 21 square fields (15 × 15 mm²) received a 160 ns laser pulse from a SCREEN LT-3100 system ($\lambda = 308$ nm) whose chuck was stabilized at 200 °C in a N₂ atmosphere. To induce different conditions of

TABLE I. Boron implant conditions and wafer labeling.

Energy – dose	Wafer labeling
3 keV – $1.5 \times 10^{16} \text{ cm}^{-2}$	W-315
3 keV – $2.5 \times 10^{16} \text{ cm}^{-2}$	W-325
4 keV – $1.5 \times 10^{16} \text{ cm}^{-2}$	W-415
4 keV – $2.5 \times 10^{16} \text{ cm}^{-2}$	W-425

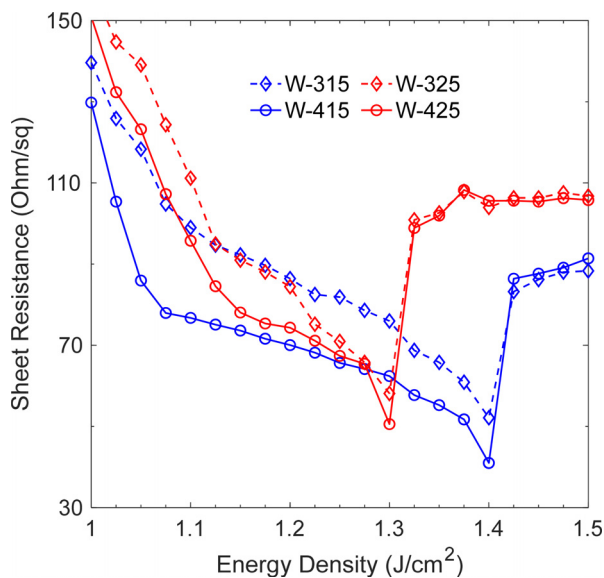
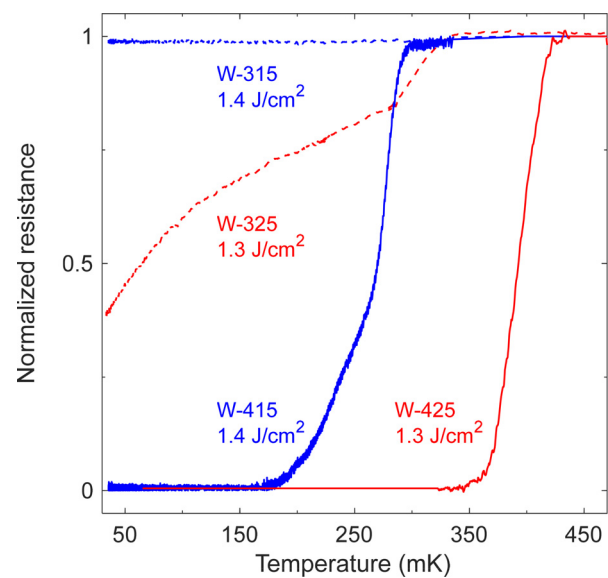
LPER, each field was annealed at a given energy density (ED) between 1.0 and 1.5 J/cm² with an energy step $\Delta_{\text{ED}} = 25 \text{ mJ/cm}^2$. After anneal, the sheet resistance of each square field was measured at 20 °C. Measurements down to 50 mK and scanning transmission electron microscopy (STEM) observations were done on 4 particular samples.

Figure 1 highlights the evolution of the sheet resistance (R_s) measured at 20 °C as a function of ED. In all wafers, increasing the ED initially leads to a sharp decrease in R_s . This drop results from the melt of the amorphous layer followed by its explosive recrystallization into doped polycrystalline Si.^{10,11} Then, the slower decrease in R_s indicates that the ED is high enough to cause a second melt after the explosive recrystallization.^{10,11} At small ED's, the second melt only affects the newly formed polycrystalline Si, leading to an increased dopant activation. At higher ED's, the second melt reaches the monocrystalline part of the SOI layer, leading after LPER to monocrystalline films of increasing thickness, and hence, decreasing R_s . When the second melt ultimately reaches the BOX, a polycrystalline film forms because there is no more seed left for LPER. This event is characterized by a sudden R_s increase between $\text{ED}_{\text{FM}} - \Delta_{\text{ED}}$ and ED_{FM} , the so-called full-melt threshold.^{6,7} One may also comment on the steep R_s decrease between $\text{ED}_{\text{FM}} - 2\Delta_{\text{ED}}$ and $\text{ED}_{\text{FM}} - \Delta_{\text{ED}}$. Our interpretation is that the second melt stops sufficiently away from the post-implantation amorphous/crystalline interface so that the growth of extended defects from the

coalescence of self-interstitials is prevented.¹² Thus, the formation of a defect-free SOI film would account for this steeper decrease in R_s .

As also outlined in Fig. 1, ED_{FM} decreases from 1.425 to 1.325 J/cm² when increasing the dose. This effect could be due to a decrease in the reflectivity of the liquid when increasing the boron content, in agreement with what has been reported in silicon-germanium alloys.¹³ One may also comment on the influence of dose and energy on the four minimum R_s (R_{315}^m , R_{325}^m , R_{415}^m , and R_{425}^m) obtained at $\text{ED}_{\text{FM}} - \Delta_{\text{ED}}$. The related doped-layers have approximately the same thickness ($\sim 30 \text{ nm}$), and the active boron concentration C_A is relatively constant within the layers because of the very rapid homogenization upon melting.⁶ Hence, the differences in R_s roughly arise from $(C_A \times \mu)^{-1}$, where μ is the hole mobility. At a given energy, $R_{315}^m < R_{325}^m$ and $R_{415}^m < R_{425}^m$. In both cases, we cannot tell which film has the higher C_A because μ is not constant. Indeed, we expect μ to decrease with the dose due to higher disorder (clusters/precipitates). It is, thus, safer to compare the R_s at a given dose: $R_{415}^m < R_{315}^m$ and $R_{425}^m < R_{325}^m$ most likely indicate that the 4 keV energy leads to an increased C_A .

Regarding superconductivity in monocrystalline Si, it has been shown that the higher the active dose (at/cm²), the higher the T_C .^{6,14} In this respect, the energy density $\text{ED}_{\text{FM}} - \Delta_{\text{ED}}$ allows to reach a maximum active dose while preserving the monocrystalline quality of the SOI layer. Superconductivity is then assessed in the four films annealed in this particular condition (Fig. 2). While premises of superconductivity are evidenced in the curve related to W-325, both 4 keV-implanted films are superconducting with a T_C that increases with dose from 270 to 390 mK. As compared to the previous study,⁷ increasing the implant energy by only one keV enables superconductivity below the full melt threshold and makes the T_C increase from 170 mK to a maximum of 390 mK. This result corroborates the previously reached conclusion that 4 keV implants lead to an increased boron activation at $\text{ED}_{\text{FM}} - \Delta_{\text{ED}}$. Moreover, increasing the dose either

**FIG. 1.** 20 °C Sheet resistance as a function of energy density. Lines are guides for the eye.**FIG. 2.** Normalized resistance of films annealed at $\text{ED}_{\text{FM}} - \Delta_{\text{ED}}$ (Fig. 1) vs temperature. The T_C is extracted at normalized resistance = 0.5.

promotes superconductivity (3 keV) or leads to an increase in the T_C (4 keV). We conclude that highest-dose films feature higher active doses even though they are more resistive (Fig. 1). As discussed earlier, this conclusion is not contradictory and is in line with similar studies (e.g., Fig. 3.21 in Ref. 15).

Cross-sectional STEM images of films annealed at $ED_{FM}-\Delta_{ED}$ are shown in Fig. 3. The high angle annular dark-field imaging technique was employed to put in light variations in the atomic number. Tiny dark spots, indicative of boron precipitates, can be seen at the surface of the film related to W-315. Precipitates are better resolved in films related to W-325 and W-425, with a higher density of them in the former. We conclude that 3 keV-implanted films are more sensitive to precipitation than 4 keV-implanted ones at a given dose. This result corroborates the fact that 3 keV-implanted films are more resistive (Fig. 1) and are not superconducting (Fig. 2). Furthermore, fast Fourier transform (FFT) measurements were carried on high-resolution images for each film. All recorded images are similar to the ones shown in Fig. 3 insets, in which a single lattice is observed. We conclude that SOI films are indeed monocrystalline.

In the following, we present a model accounting for boron precipitation upon laser anneal. First, we rule out the possibility of precipitation from a solid solution since the diffusion length upon such short anneal is meaningless ($< 1 \text{ \AA}$).¹⁶ Second, we consider that precipitation does not start upon the very sudden primary melt (few ns).¹⁷ To derive the atomic fraction of boron in the second melt (X_0), we make the approximation that the as-implanted profile follows a Gaussian distribution of mean μ , standard deviation σ , and peaks concentration $\frac{\phi}{\sqrt{2\pi}\sigma}$, where ϕ is the dose. From simulations, $\mu = 9.9$, $\sigma = 4 \text{ nm}$ for a 3 keV boron implant, and $\mu = 13.2$, $\sigma = 5.4 \text{ nm}$ for a 4 keV boron implant.¹⁸ Upon melting, the extremely high boron diffusivity in liquid Si ($\sim 10^{-4} \text{ cm}^2/\text{s}$) results in the almost-instantaneous homogenization of the concentration (e.g., Fig. 3 in Ref. 19). Hence, we obtain the

following expression by assuming that X_0 is constant throughout the melt,

$$X_0(x_L) = \frac{\int_0^{x_L} C_B(x) dx}{x_L C_S + \int_0^{x_L} C_B(x) dx}, \quad (1)$$

where x_L is the depth of the advancing liquid/solid (L/S) interface, C_S the concentration of atoms in Si ($5 \times 10^{22} \text{ at/cm}^3$) and $C_B(x)$ the as-implanted boron concentration at a depth x . The evolution of X_0 with x_L is shown in Fig. 4. X_0 increases as the liquid gets thicker until it reaches a maximum at $x_L = \mu + \sigma$. Then, X_0 decreases as less and less boron is introduced into the advancing melt. Clearly, increasing the implantation energy at a given dose makes the solution less enriched with boron upon the spreading of the second melt. This is due to the broader shape of the as-implanted profile.

Because x_L remains small ($< 30 \text{ nm}$), we consider that the temperature is uniform inside the melt (e.g., Fig. 3 in Ref. 19). Furthermore, if we refer to the phase diagram, the melting temperature of the liquid evolves slightly (1385°C – 1414°C) in the range of boron fraction 0–15 at. %.²⁰ Hence, we make the approximation that the liquid is at the Si melting point ($T_M = 1414^\circ\text{C}$). The corresponding solubility limit X_z^* is drawn in Fig. 4. According to the model, precipitation occurs beyond a critical x_L ($X_0 > X_z^*$) at the exception of the film related to W-415. At a given dose, a more pronounced precipitation is expected in 3 keV-implanted films because of the higher gap between X_0 and X_z^* . Both predictions are consistent with observations (Fig. 3).

The precipitates growth rate is assessed as follows. The phase to consider is SiB_3 , as it is known to grow from boron-saturated solution in both the solid and the liquid states.²¹ Assuming a diffusion-limited reaction, the growth rate of spherical precipitates is given by Zener *et al.*,²²

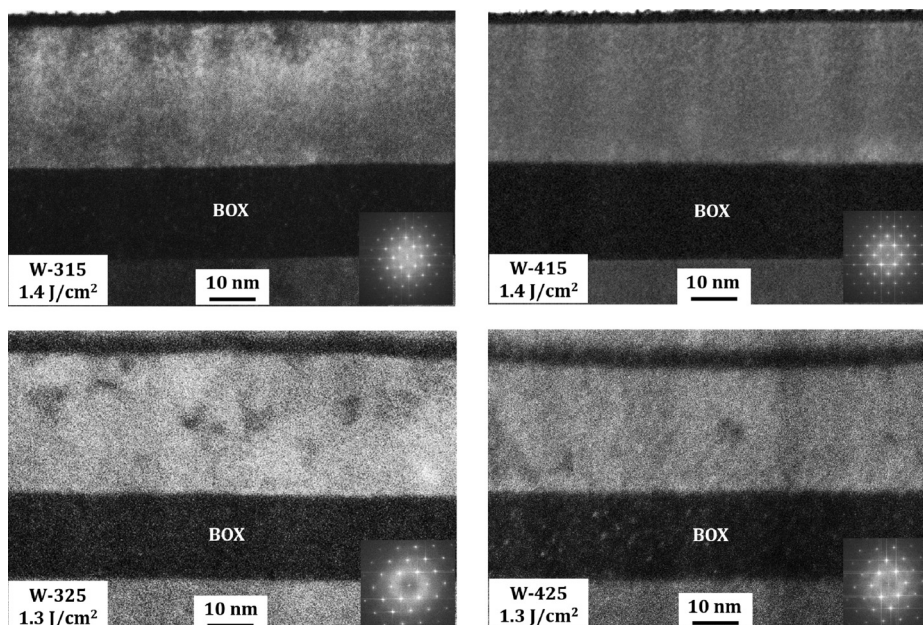


FIG. 3. Cross-sectional STEM images of films annealed at $ED_{FM}-\Delta_{ED}$. Fast Fourier transform of high-resolution images is shown in the insets.

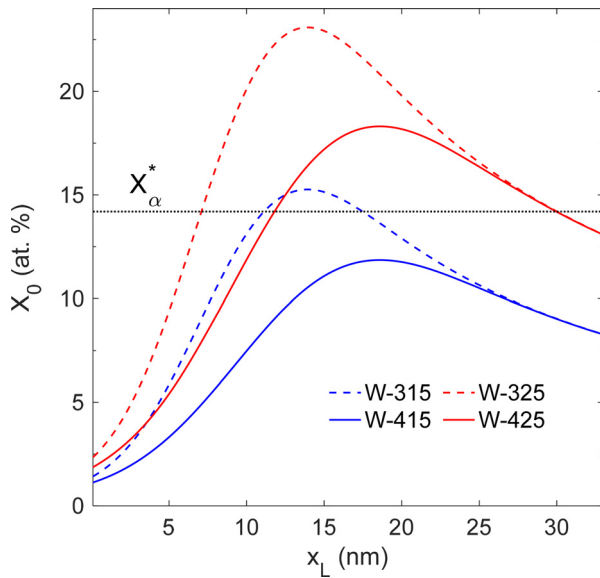


FIG. 4. The atomic fraction of boron in the liquid as a function of the depth of the advancing L/S interface. The solubility limit of boron in liquid Si at T_M ($X_\alpha^* = 14.2$ at. %) is indicated by a black dotted line.

$$\frac{dR_p}{dt} = \frac{X_\alpha^F - X_\alpha^*}{2X_\beta - X_\alpha^*} \times \frac{D}{R_p}, \quad (2)$$

where R_p is the radius of precipitates, D is the diffusivity of boron in liquid Si (1.2×10^{-4} cm²/s),²³ X_α^F is the atomic fraction of boron in the liquid far away from precipitates, and X_β is the one in SiB₃ (75 at. %). The factor 2 comes from the ratio between the concentration of atoms in precipitates ($\sim 10^{23}$ at/cm³)²⁴ and the one in the liquid phase ($\sim 5 \times 10^{22}$ at/cm³).²⁵ At the beginning of precipitation, it is common practice to assume that the liquid far from precipitates is not affected by the growth ($X_\alpha^F = X_0$). When X_0 remains constant over growth, this relation does not hold long because boron is pumped further and further from precipitates. Here, we considered that $X_\alpha^F = X_0$ is a good approximation in the thickness range $[0, \mu + \sigma]$ because X_0 increases at the same time as precipitation occurs. Finally, we used $t = x_L/v_s$ for the growth time, where $v_s = 0.3$ m/s is the velocity of the L/S interface estimated from time-resolved-reflectometry.^{6,7}

Using the previous assumptions, Eq. (2) has been numerically integrated between t_0 and t_F , where t_0 is the time at which X_0 becomes higher than X_α^* (Fig. 3) and t_F the time at which X_0 reaches its maximum at $x_L = \mu + \sigma$. The calculated R_p can be compared to the mean size of precipitates R_E measured in STEM images (Fig. 3). Such measurements could not be performed in the film related to W-315 because the dark spots are not well defined. As outlined in Table II, R_S and R_E are relatively close to one another. This tends to indicate that precipitation completes around t_F . The fact that precipitates are mostly evidenced in the first $\mu + \sigma$ nm (14 or 19 nm) corroborates this interpretation (Fig. 3). At least it seems reasonable to conclude that precipitation completes before the onset of LPER ($x_L \sim 30$ nm) in films annealed at $ED_{FM} - \Delta_{ED}$.

In order to estimate the fraction of the dose trapped in precipitates F_p , let us assume that precipitation ends the very moment the L/S

TABLE II. Calculated radius (R_p) vs experimental size (R_E) of precipitates. NP = no precipitation.

Film label	R_p (nm)	R_E (nm)
W-315 1.4 J/cm ²	1.1	/
W-325 1.3 J/cm ²	4.9	3.1
W-415 1.4 J/cm ²	NP	NP
W-425 1.3 J/cm ²	3.3	2.2

interface reaches $x_L = \mu + \sigma$. F_p is related to the molar fraction of precipitates as given as follows:²⁶

$$F_p = 0.84 \frac{X_\beta}{X_0} \frac{X_0 - X_\alpha^*}{X_\beta - X_\alpha^*}, \quad (3)$$

where $X_0(\mu + \sigma)$ is known from Eq. (1). The factor 0.84 accounts for the fact that only 84% of the dose is comprised in the melt. Then, we can deduce the dose available for LPER (D_L), that is the dose present in the liquid phase when the L/S interface reached its deepest position ($x_L \sim 30$ nm in films annealed at $ED_{FM} - \Delta_{ED}$). Results are shown in Table III. According to the model, around 40% of the dose is consumed by precipitation in the film related to W-325. As a result, the corresponding D_L is equal to the one of W-415, in which precipitation has not occurred. The highest D_L is found in the film featuring the best compromise between high implanted dose and low F_p , namely, the film related to W-425. Hence, increasing the implantation energy helps reducing precipitation during the melting phase, thus leading to a higher boron dose available for activation at the onset of LPER.

Finally, we can deduce the dose retained in the epitaxial layer after LPER, namely, $k_s \times D_L$, where k_s is the segregation coefficient of boron in Si. This latter is close to 0.85 in our experimental conditions ($v_s \sim 0.3$ m/s).²⁷ In 4 keV-implanted films, we, thus, find that the retained dose is close to 1.3×10^{16} and 1.6×10^{16} at/cm², respectively. According to GILD experiments,¹⁴ such doses would lead to T_C of 280 and 380 mK, in excellent agreement with what is actually found (270 and 390 mK). This means that the model, despite its simplicity, lead to accurate predictions in this case. However, the model fails in predicting the non-superconducting behavior of 3 keV-implanted films: the retained doses seem too high. We believe that the amount of boron trapped in precipitates is underestimated at this energy, probably because the as-implanted profiles determined from the Gaussian assumption are incorrect. Note also that further increase in the T_C requires higher retained doses. In this respect, shorter laser pulses (e.g., 25 ns)⁶ are needed to reduce the precipitation time (smaller F_p) and increase the solidification velocity ($k_s \sim 1$).

TABLE III. F_p and D_L in films annealed at $ED_{FM} - \Delta_{ED}$ assuming that precipitation completes a $x_L = \mu + \sigma$.

Film label	F_p (%)	D_L (at/cm ²)
W-315 1.4 J/cm ²	7	1.4×10^{16}
W-325 1.3 J/cm ²	40	1.5×10^{16}
W-415 1.4 J/cm ²	0	1.5×10^{16}
W-425 1.3 J/cm ²	23	1.9×10^{16}

In summary, we have studied the effect of boron implant dose and energy on the superconductivity of laser-annealed monocrystalline SOI films (~ 30 nm). Despite the extremely short duration of laser pulses (160 ns), we have shown that boron precipitation could still occur in the liquid phase due to the very high concentrations generated by ion implantation. Such effects can be alleviated if not suppressed by using a 4 keV instead of a 3 keV implant energy, the implanted dose being distributed over a larger depth. In doing so, monocrystalline SOI films with relatively high T_C (390 mK) have been obtained. The combination of 4 keV ion implantation and nanosecond laser anneal below the full melt threshold is compatible with the 300 mm-manufacturing of all-silicon Josephson junctions.

The authors would like to thank SCREEN company and its French subsidiary LASSE for helping in operating and maintaining the LT-3100 laser annealing system. This work was founded by European projects MATQu and SIQUOS (Grant Agreement Nos. 101007322 and 101017733).

AUTHOR DECLARATIONS

Conflict of Interest

The authors have no conflicts to disclose.

Author Contributions

Paul Dumas: Conceptualization (supporting); Writing – original draft (supporting). **Mathieu Opprecht:** Conceptualization (equal); Formal analysis (equal); Resources (equal). **Sébastien Kerdiles:** Formal analysis (supporting); Investigation (supporting); Methodology (supporting). **Janos L. Labar:** Investigation (lead); Methodology (supporting); Validation (supporting). **Bela Pecz:** Investigation (lead); Methodology (supporting); Validation (supporting). **François Lefloch:** Investigation (lead); Methodology (equal); Supervision (lead). **Fabrice Nemouchi:** Conceptualization (supporting); Investigation (supporting); Project administration (supporting); Supervision (lead).

DATA AVAILABILITY

The data that support the findings of this study are available within the article.

REFERENCES

- M. H. Devoret and R. J. Schoelkopf, "Superconducting circuits for quantum information: An outlook," *Science* **339**(6124), 1169–1174 (2013).
- M. Kjaergaard, M. E. Schwartz, J. Braumüller, P. Krantz, J. I. J. Wang, S. Gustavsson, and W. D. Oliver, "Superconducting qubits: Current state of play," *Annu. Rev. Condens. Matter Phys.* **11**, 369–395 (2020).
- F. Arute, K. Arya, R. Babbush, D. Bacon, J. C. Bardin, R. Barends *et al.*, "Quantum supremacy using a programmable superconducting processor," *Nature* **574**(7779), 505–510 (2019).
- F. Chiodi, J. E. Duvauchelle, C. Marcenat, D. Débarre, and F. Lefloch, "Proximity-induced superconductivity in all-silicon superconductor/normal-metal junctions," *Phys. Rev. B* **96**(2), 024503 (2017).
- E. Bustarret, C. Marcenat, P. Achatz, J. Kačmarčík, F. Lévy, A. Huxley *et al.*, "Superconductivity in doped cubic silicon," *Nature* **444**(7118), 465–468 (2006).
- F. Chiodi, R. Daubriac, and S. Kerdiles, "Laser ultra-doped silicon: Superconductivity and applications," in *Laser Annealing Processes in Semiconductor Technology* (Woodhead Publishing, 2021), pp. 357–400.
- R. Daubriac, P. A. Alba, C. Marcenat, S. Lequien, T. D. Vethaak, F. Nemouchi *et al.*, "Superconducting polycrystalline silicon layer obtained by boron implantation and nanosecond laser annealing," *ECS J. Solid State Sci. Technol.* **10**(1), 014004 (2021).
- C. Huang and T. Duzer, "Single-crystal silicon-barrier Josephson junctions," *IEEE Trans. Magn.* **11**(2), 766–769 (1975).
- S. Graser, P. J. Hirschfeld, T. Kopp, R. Gutser, B. M. Andersen, and J. Mannhart, "How grain boundaries limit supercurrents in high-temperature superconductors," *Nat. Phys.* **6**(8), 609–614 (2010).
- S. Kerdiles, P. A. Alba, B. Mathieu, M. Veillerot, R. Kachtouli, P. Besson *et al.*, "Dopant activation and crystal recovery in arsenic-implanted ultra-thin silicon-on-insulator structures using 308 nm nanosecond laser annealing," in *16th International Workshop on Junction Technology (IWJT)* (IEEE, 2016), pp. 72–75.
- N. Chery, M. Zhang, R. Monflier, N. Mallet, G. Seine, V. Paillard *et al.*, "Study of recrystallization and activation processes in thin and highly doped silicon-on-insulator layers by nanosecond laser thermal annealing," *J. Appl. Phys.* **131**(6), 065301 (2022).
- Y. Qiu, F. Cristiano, K. Huet, F. Mazzamuto, G. Fisicaro, A. La Magna *et al.*, "Extended defects formation in nanosecond laser-annealed ion implanted silicon," *Nano Lett.* **14**(4), 1769–1775 (2014).
- D. Ricciarelli, G. Mannino, I. Deretzis, G. Calogero, G. Fisicaro, R. Daubriac *et al.*, "Impact of surface reflectivity on the ultra-fast laser melting of silicon-germanium alloys," *Mater. Sci. Semicond. Process.* **165**, 107635 (2023).
- A. Grockowiak, T. Klein, H. Cercellier, F. Lévy-Bertrand, X. Blase, J. Kačmarčík *et al.*, "Thickness dependence of the superconducting critical temperature in heavily doped Si:B epilayers," *Phys. Rev. B* **88**(6), 064508 (2013).
- L. Desvignes, "Laser doped superconducting silicon: From the material to the devices," Doctoral dissertation (Université Paris-Saclay, 2023).
- P. Pichler, *Intrinsic Point Defects, Impurities, and Their Diffusion in Silicon* (Springer Science & Business Media, 2012).
- S. F. Lombardo, S. Boninelli, F. Cristiano, I. Deretzis, M. G. Grimaldi, K. Huet *et al.*, "Phase field model of the nanoscale evolution during the explosive crystallization phenomenon," *J. Appl. Phys.* **123**(10), 105105 (2018).
- Ion Implantation: Projected Range & Straggle Calculator, see <https://cleanroom.byu.edu/rangestruggle> for "Integrated Microfabrication Lab (Cleanroom)."
- G. Fisicaro, K. Huet, R. Negru, M. Hackenberg, P. Pichler, N. Taleb, and A. La Magna, "Anomalous impurity segregation and local bonding fluctuation in *l*-Si," *Phys. Rev. Lett.* **110**(11), 117801 (2013).
- R. W. Olesinski and G. J. Abbaschian, "The B–Si (Boron-Silicon) system," *Bull. Alloy Phase Diagrams* **5**(5), 478–484 (1984).
- T. L. Aselage, "The coexistence of silicon borides with boron-saturated silicon: Metastability of SiB₃," *J. Mater. Res.* **13**(7), 1786–1794 (1998).
- C. Zener, "Theory of growth of spherical precipitates from solid solution," *J. Appl. Phys.* **20**(10), 950–953 (1949).
- K. Tang, E. J. Øvrelid, G. Tranell, and M. Tangstad, "Critical assessment of the impurity diffusivities in solid and liquid silicon," *JOM* **61**, 49–55 (2009).
- D. Eklöf, A. Fischer, A. Ektarawong, A. Jaworski, A. J. Pell, J. Grins *et al.*, "Mysterious SiB₃: Identifying the relation between α - and β -SiB₃," *ACS Omega* **4**(20), 18741–18759 (2019).
- K. Mukai and Z. Yuan, "Measurement of the density of molten silicon by a modified sessile drop method," *Mater. Trans., JIM* **41**(2), 323–330 (2000).
- T. Philippe, F. De Geuser, S. Duguay, W. Lefebvre, O. Cojocar-Mirélin, G. Da Costa, and D. Blavette, "Clustering and nearest neighbour distances in atom-probe tomography," *Ultramicroscopy* **109**(10), 1304–1309 (2009).
- R. F. Wood, "Model for nonequilibrium segregation during pulsed laser annealing," *Appl. Phys. Lett.* **37**(3), 302–304 (1980).